

that include, for example, citron kinase, MKLP1/CHO1, and HIP1 (59–61). Ancient and common pathways may function to establish and maintain membrane-cytoskeletal dynamics in different cell types and organisms. Fourteen percent of the mammalian proteins identified in this study are implicated in human diseases with membrane-cytoskeletal pathologies, such as Huntington's disease, deafness, sclerosis, melanoma, and leukemia (62–66), suggesting that functional characterization of cell division proteins may help to identify mammalian disease loci and characterize pathologies. The utilization of common components in diverse dynamic membrane cytoskeletal events in the cleavage furrow, the germline, and neurons indicates ancient mechanisms mediating cell division and complex morphogenetic cellular processes critical in human development and disease.

## References and Notes

1. K. N. Bhalla, *Oncogene* **22**, 9075 (2003).
2. M. Carmena, W. C. Earnshaw, *Nat. Rev. Mol. Cell Biol.* **4**, 842 (2003).
3. W. Flemming, *Arch. Mikrosk. Anat.* **37**, 685 (1891).
4. N. Paweletz, *Nat. Rev. Mol. Cell Biol.* **2**, 72 (2001).
5. J. M. Mullins, J. R. McIntosh, *J. Cell Biol.* **94**, 654 (1982).
6. A. A. Hyman, *J. Cell Biol.* **109**, 1185 (1989).
7. K. Dan, Y. Tanaka, *Ann. N. Y. Acad. Sci.* **582**, 108 (1990).
8. A. R. Skop, J. G. White, *Curr. Biol.* **8**, 1110 (1998).
9. R. K. Miller, S. C. Cheng, M. D. Rose, *Mol. Biol. Cell* **11**, 2949 (2000).
10. C. Sellitto, R. Kuriyama, *J. Cell Biol.* **106**, 431 (1988).
11. S. P. Wheatley, S. E. Kandels-Lewis, R. R. Adams, A. M. Ainsztein, W. C. Earnshaw, *Exp. Cell Res.* **262**, 122 (2001).
12. C. Mollinari et al., *J. Cell Biol.* **157**, 1175 (2002).
13. T. Lang et al., *EMBO J.* **20**, 2202 (2001).
14. I. N. Fleming, C. M. Elliott, J. H. Exton, *J. Biol. Chem.* **271**, 33067 (1996).
15. A. J. Link et al., *Nat. Biotechnol.* **17**, 676 (1999).
16. J. Pickett-Heaps, S. E. Kowalski, *Eur. J. Cell Biol.* **25**, 150 (1981).
17. S. H. Brawley, R. S. Quatranro, R. Wetherbee, *J. Cell Sci.* **24**, 275 (1977).
18. N. Bieliavsky, M. Geuskens, *J. Submicrosc. Cytol. Pathol.* **22**, 445 (1990).
19. J. Matuliene, R. Kuriyama, *Mol. Biol. Cell* **13**, 1832 (2002).
20. R. S. Kamath et al., *Nature* **421**, 231 (2003).
21. A. G. Fraser et al., *Nature* **408**, 325 (2000).
22. P. Gonczy et al., *Nature* **408**, 331 (2000).
23. I. Maeda, Y. Kohara, M. Yamamoto, A. Sugimoto, *Curr. Biol.* **11**, 171 (2001).
24. M. Won et al., *Biochem. Biophys. Res. Commun.* **282**, 10 (2001).
25. P. Seidl, R. Huettinger, R. Knuechel, L. A. Kunz-Schughart, *Int. J. Cancer* **102**, 129 (2002).
26. A. Peyril, R. Weitzdoerfer, T. Gulesserian, M. Fountoulakis, G. Lubec, *Electrophoresis* **23**, 152 (2002).
27. J. C. Sisson, W. F. Rothwell, W. Sullivan, *Cell Biol. Int.* **23**, 871 (1999).
28. F. Piano, A. J. Schetter, M. Mangone, L. Stein, K. J. Kemphues, *Curr. Biol.* **10**, 1619 (2000).
29. M. Velichkova et al., *Cell Motil. Cytoskelet.* **51**, 147 (2002).
30. F. Chang, *Cell Struct. Funct.* **26**, 539 (2001).
31. L. M. Machesky, *Curr. Biol.* **8**, R202 (1998).
32. M. A. Osman, R. A. Cerione, *J. Cell Biol.* **142**, 443 (1998).
33. K. Simons, E. Ikonen, *Nature* **387**, 569 (1997).
34. E. Ikonen, *Curr. Opin. Cell Biol.* **13**, 470 (2001).
35. V. Wachtler, S. Rajagopalan, M. K. Balasubramanian, *J. Cell Sci.* **116**, 867 (2003).
36. E. B. Babychuk, A. Draeger, *J. Cell Biol.* **150**, 1113 (2000).
37. C. J. Merrifield, M. E. Feldman, L. Wan, W. Almers, *Nat. Cell Biol.* **4**, 691 (2002).
38. N. Li et al., *Proteomics* **3**, 536 (2003).
39. H. M. Thompson, A. R. Skop, U. Euteneuer, B. J. Meyer, M. A. McNiven, *Curr. Biol.* **12**, 2111 (2002).
40. B. Feng, H. Schwarz, S. Jesuthasan, *Exp. Cell Res.* **279**, 14 (2002).
41. P. E. Kuwabara, M. H. Lee, T. Schedl, G. S. Jefferis, *Genes Dev.* **14**, 1933 (2000).
42. A. R. Skop, D. Bergmann, W. A. Mohler, J. G. White, *Curr. Biol.* **11**, 735 (2001).
43. L. A. Staehelin, P. K. Hepler, *Cell* **84**, 821 (1996).
44. M. Glotzer, *Annu. Rev. Cell Dev. Biol.* **17**, 351 (2001).
45. A. Nebenfuhr, J. A. Frohlick, L. A. Staehelin, *Plant Physiol.* **124**, 135 (2000).
46. J. M. Lucocq, E. G. Berger, G. Warren, *J. Cell Biol.* **109**, 463 (1989).
47. S. Y. Bednarek, T. G. Falbel, *Traffic* **3**, 621 (2002).
48. D. Peretti, L. Peris, S. Rosso, S. Quiroga, A. Caceres, *J. Cell Biol.* **149**, 141 (2000).
49. M. Gotta, J. Ahringer, *Nat. Cell Biol.* **3**, 297 (2001).
50. W. C. Earnshaw, C. A. Cooke, *J. Cell Sci.* **98**, 443 (1991).
51. G. L. Koch, *J. Cell Sci.* **87**, 491 (1987).
52. N. Girardot et al., *Neuropathol. Appl. Neurobiol.* **29**, 451 (2003).
53. M. Jiang et al., *Biochem. Biophys. Res. Commun.* **309**, 196 (2003).
54. L. Rajendran et al., *Proc. Natl. Acad. Sci. U.S.A.* **100**, 8241 (2003).
55. E. C. Breen, K. Tang, *J. Cell. Biochem.* **88**, 848 (2003).
56. F. Lafont, K. Simons, *Proc. Natl. Acad. Sci. U.S.A.* **98**, 3180 (2001).
57. D. C. Thurmond, J. E. Pessin, *Mol. Membr. Biol.* **18**, 237 (2001).
58. L. H. Chamberlain, G. W. Gould, *J. Biol. Chem.* **277**, 49750 (2002).
59. J. P. Aumais et al., *J. Cell Sci.* **116**, 1991 (2003).
60. J. J. LoTurco, M. R. Sarkisian, L. Cosker, J. Bai, *Cereb. Cortex* **13**, 588 (2003).
61. D. J. Sharp, R. Kuriyama, R. Essner, P. W. Baas, *J. Cell Sci.* **110**, 2373 (1997).
62. H. W. Walling, J. J. Baldassare, T. C. Westfall, *J. Neurosci. Res.* **54**, 301 (1998).
63. S. Melchionda et al., *Am. J. Hum. Genet.* **69**, 635 (2001).
64. R. Brandt, *Cell Tissue Res.* **305**, 255 (2001).
65. J. W. Legg, C. A. Lewis, M. Parsons, T. Ng, C. M. Isacke, *Nat. Cell Biol.* **4**, 399 (2002).
66. J. Basu, M. Kundu, M. M. Rakshit, P. Chakrabarti, *Biochim. Biophys. Acta* **945**, 121 (1988).
67. We thank J. White, M. Mullins, R. Kuriyama, M. Welch, B. Mohler, K. O'Connell, E. Ralston, D. Chu, A. Severson, R. Chan, J. Banks, A. Van Hooser, K. Hagstrom, D. Reiner, and T. Wu for support during midbody isolation, RNAi analysis, and/or for reading the manuscript. We thank M. McNiven for antibodies to Dynamin II and to KHC, T. Hasson for antibody to KEAP1, and A. Caceres for antibody to KIF4. A.R.S. is supported by NIH grant F32 GM64159-01. R.H. is supported by the NIH, The Pew Charitable Trust, and The Cancer Research Coordinating Committee. B.J.M. is an investigator for the Howard Hughes Medical Institute. J.Y. and H.L. are supported by the Yeast Resource Center RR1823 and Office of Naval Research grant N00014-00-0421. This paper is dedicated to K. Van Doren.

## Supporting Online Material

www.sciencemag.org/cgi/content/full/1097931/DC1  
Materials and Methods  
Tables S1 and S2  
Movies S1 to S4  
References and Notes

16 March 2004; accepted 13 May 2004

Published online 27 May 2004;

10.1126/science.1097931

Include this information when citing this paper.

# REPORTS

## Three-Dimensional Polarimetric Imaging of Coronal Mass Ejections

Thomas G. Moran<sup>1,2\*</sup> and Joseph M. Davila<sup>1</sup>

We present three-dimensional reconstructions of coronal mass ejections (CMEs), which were obtained through polarization analysis of single-view images recorded with the use of the Large Angle and Spectrometric Coronagraph (LASCO) C2 coronagraph on board the Solar and Heliospheric Observatory (SOHO) spacecraft. Analysis of a loop-like CME shows a complex three-dimensional structure centered at 40° from the plane of the sky, moving radially at 250 kilometers/second. Reconstruction of two halo CMEs suggests that these events are expanding loop arcades.

Coronal mass ejections (CMEs) are one of the most energetic and important solar phenomena. These events propel magnetic

clouds with a mass of up to  $10^{17}$  (1) g to speeds up to 2600 km/s (2) into the heliosphere, influencing near-Earth plasma condi-

tions (space weather), causing fluctuations in the terrestrial magnetic field and in the ionospheric density, and driving auroras. These phenomena can affect the performance of satellites in Earth orbit (3), and the associated particle fluxes are an important safety concern for humans in space (4). During the record-breaking solar storms of October and November 2003, instruments on the NASA Advanced Composition Explorer space research satellite saturated because of solar particle fluxes. Radio communications were affected across the globe, and large electric currents were induced in European and American power grids because of fluctuations in the Earth's magnetic field, causing temporary outages in Europe. Because of these terrestrial and geospheric effects,

there has been an increasing interest in studying the generation and propagation of CMEs.

CMEs occur in conjunction with solar flares and filament eruptions and are understood to be driven by the conversion of magnetic energy to thermal and kinetic energy. These events, first observed in 1972 (5), have been studied primarily through the use of ground- and space-based coronagraphs. The Large Angle and Spectrometric Coronagraph (LASCO) (6), on board the Solar and Heliospheric Observatory (SOHO) (7), was launched to study these events. SOHO is located at the Lagrangian 1 point, where the Sun and Earth's gravitational fields cancel. LASCO includes two white-light imaging coronagraphs, which have allowed extensive studies of CME characteristics to a plane-of-the-sky distance of 32 solar radii ( $R_{\odot}$ ) (plane of the sky refers to the plane centered on the Sun and perpendicular to the Earth-Sun line). The major limitation of CME observations to date has been a lack of three-dimensional structure and trajectory measurements. Speed and direction measurements would allow more accurate prediction of CME impacts, which would allow better planning of protective measures, such as attitude adjustment and astronaut shielding. In addition, three-dimensional measurements would yield insight into CME generation and permit additional tests of CME dynamical models.

In the polarization analysis technique, the ratio of polarized-to-unpolarized electron-scattered emissivity (K-corona) is measured by recording coronal images through three or more polarizers with axes oriented at multiple angles. A measurement of the brightness ratio determines the line-of-sight averaged distance from the plane of the sky. In the case of an extended source, the brightness ratio will be a weighted average, characteristic of a point within the structure. We used a variation of the single-view polarization analysis technique to study the structure and position of three CMEs observed with SOHO/LASCO. The line-of-sight averaged distances from the plane of the sky are computed from measurements of the ratio of polarized-to-unpolarized brightness, providing the first topographical maps of CMEs. From these maps, we construct a view from above the ecliptic and a view from within the ecliptic, perpendicular to the Earth-Sun line. These reconstructed views yield insight into CME structure and dynamics. In addition, we can

determine the direction of CMEs and compute their true speeds, rather than the plane-of-the-sky speeds computed by measuring apparent motion of features such as loop fronts in the image frame.

The polarization of coronal electron- or Thomson-scattered solar disk continuum emission is well known (8). The fundamental cause of the polarization is the variation in scattering amplitude with the angle between the electric field vector and the scattering direction. Scattering is maximum perpendicular to the field direction. As a result of this angular dependence, a fraction of the scattered light is polarized tangential to the limb. The tangentially and radially polarized brightness components,  $I_t$  and  $I_r$ , have been calculated for a disk luminosity function of the form  $I = I_0 (1 - u + u \cos\psi)$ , where  $I_0$  is the disk center intensity,  $u$  is a wavelength-dependent constant, and  $\psi$  is the angle between the radial line segment connecting the sun center and the disk source point and the radial line segment connecting the sun center and the scattering point. The following relations yield  $I_t$  and  $I_r$ :

$$I_t = I_0 \frac{N_e \pi \sigma}{2} [(1 - u)C + uD] \quad (1)$$

$$I_t - I_r = I_0 \frac{N_e \pi \sigma}{2} \sin^2 \chi [(1 - u)A + uB] \quad (2)$$

where  $\chi$  is the angle between a radial intersecting the scattering point and the line of sight, or Earth-Sun line;  $N_e$  is the local coronal density;  $\sigma$  is the Thomson-scattering cross section; and the constants  $A$ ,  $B$ ,  $C$ , and  $D$  are functions of  $\Omega$ , the half-angle subtended by the disk at the scattering point (9, 10). This angle  $\Omega$  is a function of the heliocentric distance,  $r$ . The polarized and unpolarized brightnesses,  $I_p$  and  $I_u$ , are given by

$$I_p = I_t - I_r \quad (3)$$

$$I_u = 2I_r \quad (4)$$

Because  $I_p$  increases with  $\sin^2 \chi$  and  $I_u$  decreases with increasing  $\sin^2 \chi$ ,  $I_p/I_u$  increases with increasing  $\sin^2 \chi$ . Beyond  $1.3R_{\odot}$ , the ratio is primarily a function of  $\chi$ , except for values of  $\chi$  near  $0^\circ$  and  $90^\circ$ , where it varies with  $r$ .

We present analyses of one loop-like CME and two Earth-directed or "halo" CMEs, so called because they appear as halos around the occulting disks. Loop-like and halo CMEs represent two views of a coronal eruption; a loop-like CME provides a side view, whereas a halo CME provides a front or rear view, depending on the direction of propagation. The loop-like CME was imaged four times on 31 October 1998 at 1-h intervals. A halo CME was imaged three times on 29 June 1999 at 2-h intervals, and another was imaged 17 times on 11 November 1998 for 17 h at

1-h intervals. Both the loop and halo observations selected were preceded by polarimetric observations made before CME initiation within the previous 2 days in order to obtain pre-CME frames for subtraction, which are required in order to remove instrumental- and dust-scattered light.

The LASCO C2 externally occulted, refracting coronagraph images the corona between  $2R_{\odot}$  and  $6R_{\odot}$  (6). Individual polarimetric exposure times were 100 s, and the total time for the three images was 300 s. Images were corrected for vignetting and an offset. The charge-coupled device frame size is  $6^\circ$  by  $6^\circ$  or  $7.7 \times 10^6$  km by  $7.7 \times 10^6$  km. Pixel size in the 1024-pixel-by-1024-pixel images is  $11.4''$ . These images were 2 pixels by 2 pixels binned on board SOHO, yielding 512 by 512 images with a pixel size of  $22.8''$ . In order to measure the ratio between the polarized and unpolarized Thomson-scattered brightness component, three separate exposures are recorded through polarizers oriented horizontally and at  $60^\circ$  above and below the horizontal axis. The 512 by 512 frames were smoothed with the use of a 5-pixel-by-5-pixel box filter to increase the signal-to-noise ratio and to compensate for object motion between individual polarized exposures. Two folding mirrors in the beam path contributed to a small instrumental elliptical polarization, which was removed with use of the Mueller matrix formalism.

The dust-scattered (F-corona) and instrument-scattered components must be removed from the image before computing polarized and unpolarized brightness. This is achieved by subtracting a pre-CME image from the image being analyzed. The subtracted image shows only the Thomson-scattered component. For example, the electron-scattered CME brightness through the polarizer oriented at  $-60^\circ$ ,  $I_{A,-}$ , is

$$I_A = I_{\text{cme},-60} - I_{o,-60} \quad (5)$$

where  $I_{\text{cme},-60}$  and  $I_{o,-60}$  are the  $-60^\circ$  polarimetric images recorded during and before the CME, respectively. The  $0^\circ$  and  $+60^\circ$  CME components,  $I_B$  and  $I_C$ , are computed in an identical manner. The polarized and unpolarized CME brightness components,  $I_{p,\text{cme}}$  and  $I_{u,\text{cme}}$ , and total brightness,  $I_{t,\text{cme}}$ , are given by (8)

$$I_{p,\text{cme}} = \frac{4}{3} [(I_A + I_B + I_C)^2 - 3(I_A I_B + I_A I_C + I_B I_C)]^{1/2} \quad (6)$$

$$I_{p,\text{cme}} = \frac{2}{3} (I_A + I_B + I_C) \quad (7)$$

$$I_{u,\text{cme}} = I_{t,\text{cme}} - I_{p,\text{cme}} \quad (8)$$

We define a coordinate system ( $x$ ,  $y$ ,  $z$ ) with origin at Sun center, where  $x$  and  $y$  are the horizontal and vertical coordinates in the

<sup>1</sup>National Aeronautics and Space Administration (NASA) Goddard Space Flight Center, Code 682.3, Greenbelt, MD 20770, USA. <sup>2</sup>Department of Physics, Catholic University of America, Washington, DC 20064, USA.

\*To whom correspondence should be addressed. E-mail: moran@morpheus.nascom.nasa.gov

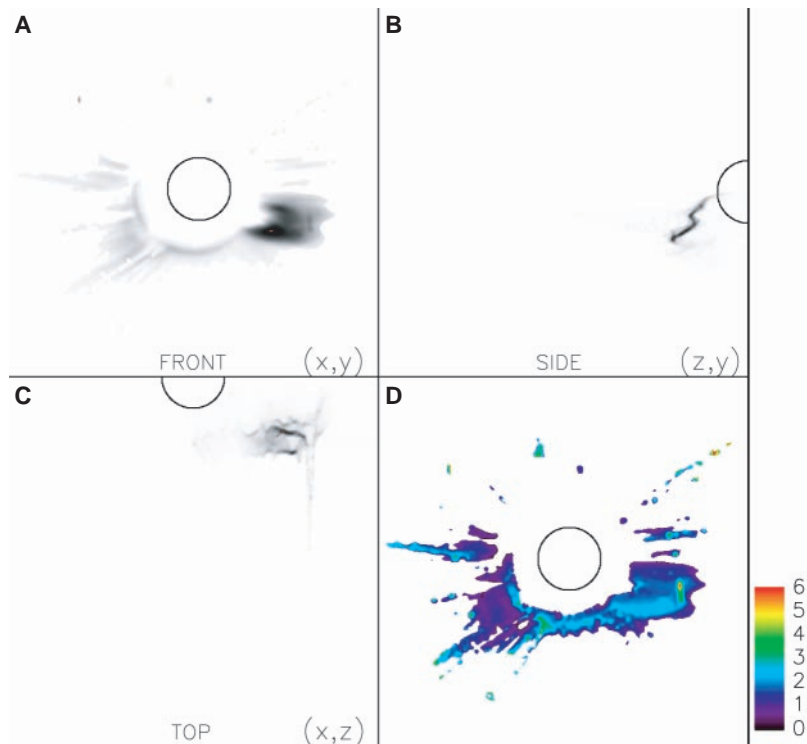


**Fig. 1.** (A) Total brightness of the loop-like CME occurring on 31 October 1998 at 3:56 UT (front view), (B) a reconstructed side view of the CME in the  $(z, y)$  plane, (C) a reconstructed top view of the CME in the  $(x, z)$  plane, and (D) a topographical map of the CME displaying distance from the  $(x, y)$  plane. The color bar indicates distance from the sky plane in  $R_{\odot}$ . The solar disk is outlined.

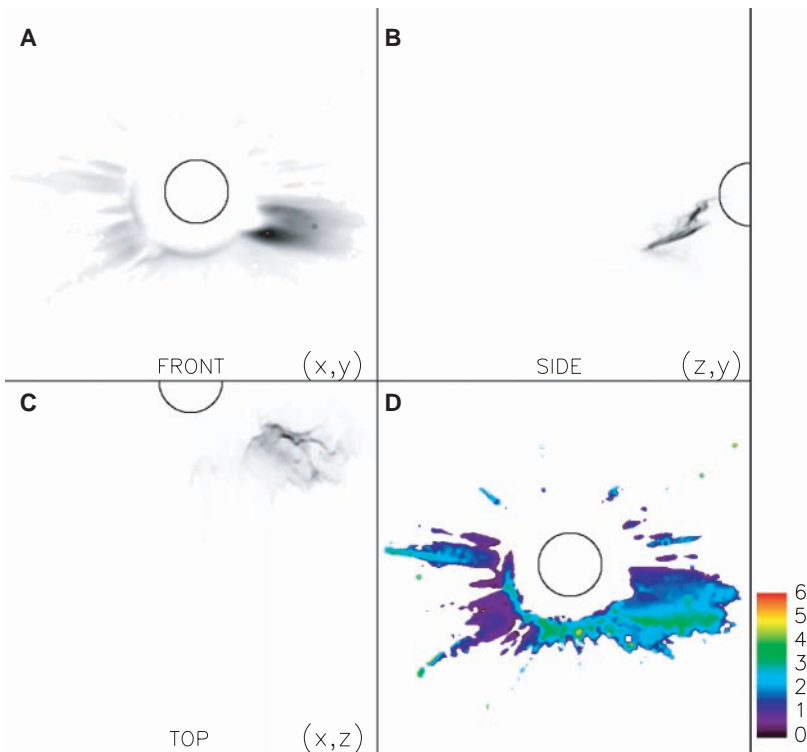


**Fig. 2.** (A) Total brightness of the loop-like CME occurring on 31 October 1998 at 4:56 UT (front view), (B) a reconstructed side view of the CME in the  $(z, y)$  plane, (C) a reconstructed top view of the CME in the  $(x, z)$  plane, and (D) a topographical map of the CME displaying distance from the  $(x, y)$  plane. The color bar indicates distance from the sky plane in  $R_{\odot}$ . The solar disk is outlined.

plane of the sky and  $z$  is the coordinate along the line of sight. The measured ratio of polarized-to-unpolarized electron-scattered brightness for a scattering point,  $r_m = I_{p,cme} / I_{u,cme}$ , must equal the theoretical ratio,  $r_t$ , which can be expressed as a function of  $\rho = \sqrt{x^2 + y^2}$  and  $|z|$ :

$$r_m = r_t(\rho, |z|) \tag{9}$$

The values of  $r_t$  are computed for a range of  $\rho$  spanning the coronagraph field of view and for an equivalent range in  $|z|$ , yielding a two-dimensional array,  $r_t$ , with  $\rho$  and  $|z|$  axes. To determine the  $|z|$  value at each CME pixel, we computed the value of  $\rho$  and extracted the corresponding column in the  $r_t$  array. Then, the  $|z|$  value along the column at which  $r_m = r_t$  is found by inspection. Because  $r_t$  is a monotonically decreasing function of  $|z|$  for all  $\rho$ , the solution is unique. The resulting  $|z|$  value is a mean distance from the plane of the sky. If there is a single object along the line of sight, the value will lie within the object, and if there are two structures along the line of sight, the value obtained will lie between the two  $|z|$  values of the two objects. The method yields a mean distance from the plane of the sky but not the sign, because the dependence of  $r_t$  on  $\sin \chi$  is quadratic: An object yields the same ratio for a given distance whether it is on the front or back of the Sun. The sign of  $\chi$  may often be determined with the use of other observations that record disk flares or filament eruptions, such as the SOHO/Extreme Ultraviolet Imaging Telescope (EIT) ultraviolet imaging instrument (11), or through measurements of bulk Doppler shifts. If there is no disk activity associated with a CME, its origin is usually on the back side.

Only  $|z|$  values for pixels with values of  $I_p$  and  $I_u$  above 5% of the mean are computed. This reduces artifacts in the three-dimensional reconstruction. The uncertainty in measuring  $\chi$  is determined by the relative error in  $r_m$ , which is estimated at 0.04. The change in  $\chi$  corresponding to a relative change in  $r_t$  of 0.04 was found by inspection for several angles. The uncertainties in  $\chi$  at 20°, 45°, and 70° were found to equal 0.21°, 2.1°, and 1.6°. Fortuitously, the uncertainty is lowest for CMEs directed along the Earth-Sun line.

The loop CME observed on 31 October 1998 was not associated with a disk event and therefore most likely originated on the back side of the Sun. A filament visible in the southwest quadrant several days before the CME was the probable source of the eruption. After subtracting binned pre-CME polarized frames recorded on the same day from the CME polarized images, the polarized, unpolarized, and total brightnesses were computed from two observation sequences 1 h apart. The total brightnesses [(x, y) plane views, Figs. 1A and 2A] show an expanding loop-

like structure in the southwest quadrant, with faint ray-like structures moving from the east limb. The blank area extending  $0.5R_{\odot}$  from the limb is in the shadow of the coronagraph occulting disk. The CME structure is diffuse, suggesting that it comprises multiple loops. The tip of the structure is dim, possibly because of lower densities at the loop apex. Topographical maps for each sequence, displaying the mean distance to the plane of the sky for each pixel in the CME (Figs. 1D and 2D), show that the bottom of the CME extends farther than the top from the plane of the sky, demonstrating its three-dimensional morphology. The maximum distances from the plane increased from  $\approx 2.5R_{\odot}$  to  $\approx 3.5R_{\odot}$  between observations. With the use of the topographical map and the total brightness image, we reconstructed views in the  $(z, y)$  (Figs. 1B and 2B) and  $(x, z)$  (Figs. 1C and 2C) planes. These reconstructions indicate a complex structure consistent with a loop or a group of loops expanding radially. The  $(x, z)$  CME views show multiple filaments, which may be shifted from their true positions because of contributions from multiple regions along the line of sight. The  $(z, y)$  views show the bottom segment expanding radially. The  $|z|$  values computed correspond to a range of  $20^{\circ}$  to  $45^{\circ}$  in angle from the plane of the sky. Other loop CMEs analyzed showed values of  $\chi$  ranging from  $10^{\circ}$  to  $70^{\circ}$ .

We compute the speed of the CME by measuring the loop front positions in the  $(x, y)$  and the  $(z, y)$  planes in both reconstructions. The speed in the  $(x, y)$  plane,  $v_p = v_x^2 + v_y^2$ , is equal to  $\Delta r/\Delta t$ , where  $\Delta r$  is the distance traveled in the  $(x, y)$  plane and  $\Delta t$  is the time interval between observations. Likewise, the speed along the Earth-Sun line ( $v_z$ ) is equal to  $\Delta z/\Delta t$ , where  $\Delta z$  is the difference between the  $|z|$  values of the loop front in the two observations. The total speed,  $v_{\text{tot}}$ , is then given by  $v_{\text{tot}}^2 = v_p^2 + v_z^2$ . We find values of  $v_p$  and  $v_z$  of 185 km/s and 167 km/s, respectively, corresponding to a  $v_{\text{tot}}$  of 250 km/s.

The effect of image motion between exposures was investigated by measuring the image shift between individual polarimetric exposures and applying a compensating shift to the individual frames. The total observation time for a polarimetric sequence was 500 s, with intervals of 100 s between exposures to transmit the images. The CME fronts moved one to two pixels between individual polarimetric exposures. It was found that the resulting  $z$  values differed from those resulting from analysis of unshifted images by less than 3%. This is explained by the fact that after binning and smoothing, the CME features are several pixels in extent. Information at scales of five pixels ( $110^{\circ}$  or 80,000 km) or less is lost by smoothing in order to determine larger scale characteristics. Examination of the  $|z|$  frame showed no discontinuities on the leading or following edges of the CMEs, where

errors due to image motion would be pronounced, indicating that the resolution was sufficient for the speeds encountered.

The halo CME observed on 29 June 1999 was associated with a front-side filament eruption at  $16^{\circ}\text{E } 20^{\circ}\text{S}$ , which was observed with the use of SOHO/EIT (11). Polarimetric observations were made 2 h after the CME began. The total brightness (Fig. 3A) shows diffuse radially oriented structures at multiple polar angles, giving a splatter-like appearance, owing to the fact that the eruption is in the direction of the instrument. The front or rear view provided by halo CMEs allows an examination of the angular structure of the eruption not possible with limb CME observations. This particular halo CME is ideal for studying the angular distribution of matter, because it is composed of distinct ray-like structures, as opposed to the solid spray of coronal material observed in some halo eruptions. The front of the eruption has moved beyond the edge of the C2 frame, indicating a  $v_p$  of at least 400 km/s.

The corresponding topographical map (Fig. 3D) shows a bilateral symmetry, with an axis oriented along a line bisecting the disk at a polar angle of  $\approx 135^{\circ}$ , measured clockwise from the north pole. The distance to the plane of the sky

is maximum along the axis of symmetry, reaching  $\approx 6R_{\odot}$ , whereas the  $|z|$  values for regions nearly perpendicular to the axis reach maxima of  $\approx 2.5R_{\odot}$ . This morphology suggests that the CME comprises a loop arcade that crosses the magnetic neutral line. The neutral line separates regions of opposite polarity magnetic flux. Magnetic field maps made with the use of the SOHO/Michelson Doppler Imager (MDI) instrument (12) show that the neutral line in the source region is approximately perpendicular to the CME symmetry axis (Fig. 3D), and in the EIT (11) Extreme Ultraviolet (EUV) images of the source region, loops spanning the line increase in brightness during CME initiation. These EUV loops are aligned with the central loops along the topographical map symmetry axis and may be the same structures in the early phase of the eruption. The two radial structures along the axis may be the legs of a loop or a group of loops oriented toward the Earth, whereas the structures at large angles to the axis may be legs of loops tilted sideways, away from the arcade center. The sideways tilt may be the result of expansion in the loop minor radius with heliocentric distance. The outer edges of the loops are not visible, because the scattering emission decreases as  $r^{-2}$  and therefore is weak at the edge of the field. In addition, the electron

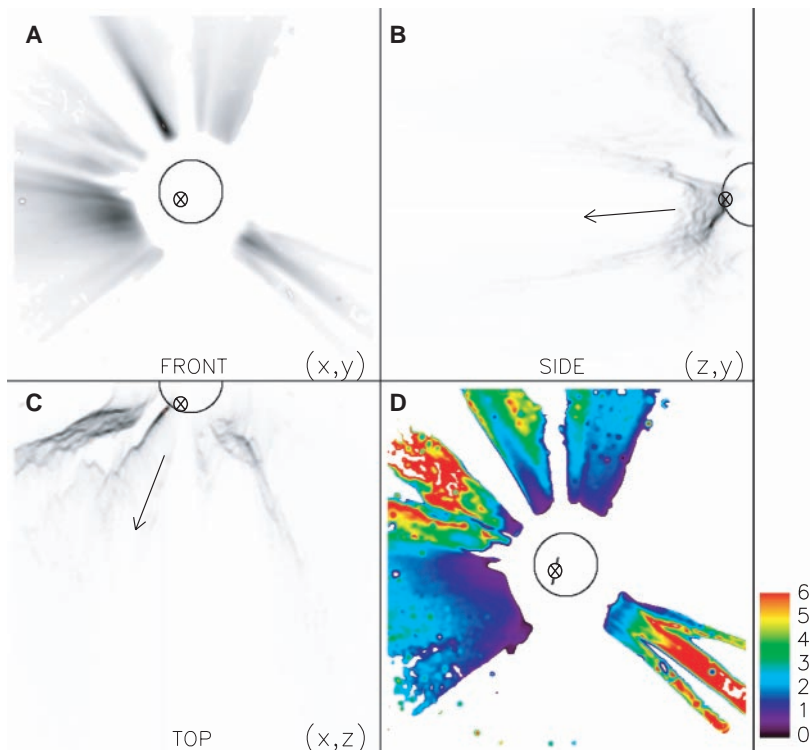


**Fig. 3.** (A) Total brightness of the halo CME occurring on 29 June 1999 (front view), (B) a reconstructed side view of the CME in the  $(z, y)$  plane, (C) a reconstructed top view of the CME in the  $(x, z)$  plane, and (D) a topographical map of the CME displaying distance from the  $(x, y)$  plane. The upper lobe in the side view is ignored because it is not part of the CME. The color bar indicates distance from the sky plane in  $R_{\odot}$ . The solar disk is outlined, and the CME source region within the disk is indicated by a  $\otimes$  symbol. An interrupted line segment through the  $\otimes$  indicates the orientation of the magnetic neutral line. Arrows in the side and top views indicate the CME direction.

density may decrease with  $r$ , contributing to the weakening of emission.

Views in the  $(z, y)$  and  $(x, z)$  planes (Fig. 3, C and D) show that the CME comprises linear structures oriented roughly radially. In the topographical map (Fig. 2D), there are at least six of these linear structures visible that remain connected to the Sun, which may be legs or groups of legs of the arcade loops. The narrow, bright structure located in the northeast quadrant was present before and after the CME and therefore was part of a different event. The loop legs have a total spread of  $\approx 90^\circ$ , consistent with many CMEs observed moving at oblique angles to the Earth-Sun line (limb CMEs). The  $(z, y)$  view shows that the legs intersect at the source region. Because the legs are distributed over most of the polar angle range and remain connected to the source region, the reconstruction suggests the CME is an expanding loop arcade, rather than a single flux rope. In the flux rope scenario, the structure remains connected to the Sun at the rope ends, rather than at multiple points along the line perpendicular to the symmetry axis, as found through our three-dimensional reconstruction. Because the bottom portions of the legs are fixed, the image motion between individual polarimetric exposures is expected to be negligible for the purpose of computing the polarized brightness.

The direction of motion found by bisecting the legs is consistent with radial motion from the source region. The CME is directed at an angle  $\chi$  of  $22^\circ$  from the line of sight. Knowing  $\chi$ , we may compute the speed along the Earth-Sun line from a measurement of the plane of the sky speed. The speed in the plane of the sky was measured at 472 km/s in the eastern lobe (2). The speed along the Earth-Sun line equals the plane-of-sky speed multiplied by the tangent of the angle between the CME direction and the line of sight, or 1090 km/s.

The halo CME observed on 4 November 1998 originated in an active region located at  $0^\circ\text{W } 20^\circ\text{N}$ . The total brightness 2 h after initiation, at a time when the CME front had moved beyond the frame edge (Fig. 4A), shows emission at all polar angles, indicating motion closely aligned with the Earth-Sun line. As in the case of the halo CME on 29 June 1999 (Fig. 3, A to D), the corresponding topographical map (Fig. 4D) shows a bilateral symmetry, with an axis oriented at  $\approx 170^\circ$  from the north pole, measured in the clockwise direction. The CME material is distributed at all polar angles, suggesting that the eruption comprises many loops, which explains its filled-in appearance. Because of this, it is difficult to determine the direction of motion by bisecting its legs. The reconstructed view in the  $(z, y)$  plane (Fig. 4B)

shows a spread in the ray-like structures of  $\approx 90^\circ$ , consistent with the CME observed on 29 June 1999. The reconstructed view in the  $(x, z)$  plane (Fig. 4C) shows complex filaments.

Maximum  $|z|$  values of  $\approx 6R_\odot$  are found at angles close to the symmetry axis, whereas the values perpendicular to it are  $\approx 3R_\odot$ . The analysis suggests that the CME is also an expanding arcade, with an axis oriented at  $\approx 80^\circ$  from the north pole, measured in a clockwise direction. The region along the symmetry axis may comprise loops directed along the Earth-Sun line, whereas the regions perpendicular to the axis may comprise loops tilted sideways. As in the case of the CME on 29 June 1999, the topographical map symmetry axis is perpendicular to the magnetic neutral line (Fig. 4D) identified in the MDI magnetic field maps (12). In addition, EIT (11) EUV images showed that at the time of the eruption, loops belonging to an arcade oriented along the symmetry axis also increased in brightness, suggesting that these or others in the same arcade expand to form the CME. If so, it may be possible to determine the direction of the field in the CME as it propagates to the Earth as a magnetic cloud. Five other halo CMEs observed in polarized emission were analyzed to determine their three-dimensional structures, which also displayed bilateral symmetry consistent with a splayed arcade morphology.

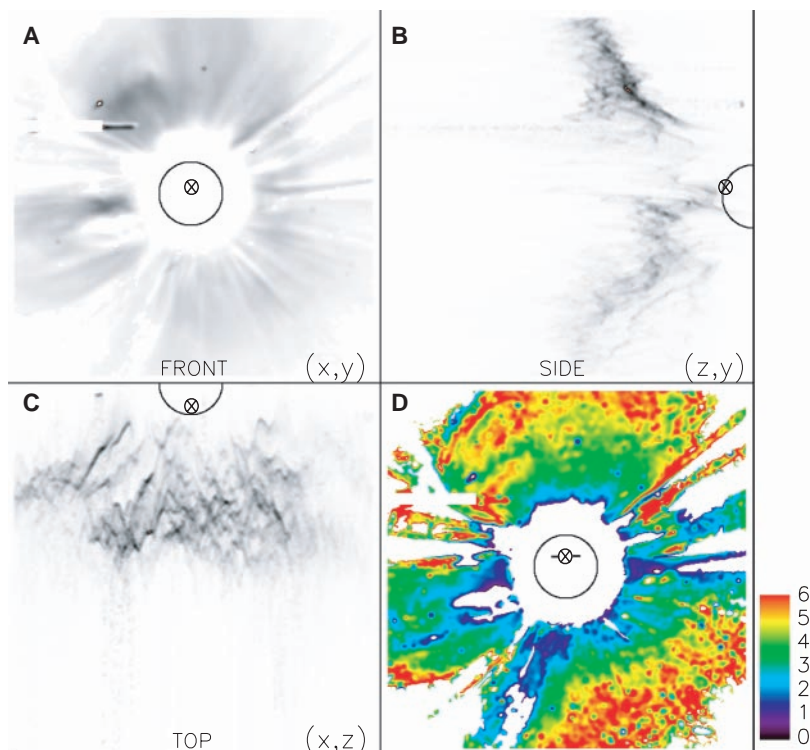


**Fig. 4.** (A) Total brightness of the halo CME occurring on 4 November 1998 (front view), (B) a reconstructed side view of the CME in the  $(z, y)$  plane, (C) a reconstructed top view of the CME in the  $(x, z)$  plane, and (D) a topographical map of the CME displaying distance from the  $(x, y)$  plane. The color bar indicates distance from the sky plane in  $R_\odot$ . The solar disk is outlined, and the CME source region within the disk is indicated by a  $\otimes$  symbol. An interrupted line segment through the  $\otimes$  symbol indicates the orientation of the magnetic neutral line.

**References and Notes**

1. A. Vourlidas, D. Buzasi, R. Howard, E. Esfandiari, in *Solar Variability from Core to Outer Frontiers—Proceedings of the 10th European Solar Physics Meeting*, Prague, Czech Republic 9 to 14 September (European Space Agency Special Publication 506, Paris, 2002), p. 91.
2. S. Yashiro et al., *J. Geophys. Res.*, in press.
3. L. Lanzerotti, in *Space Weather [Geophys. Monogr. Am. Geophys. Union 125 (2001)]*, p. 11.
4. R. Turner, in *Space Weather [Geophys. Monogr. Am. Geophys. Union 125 (2001)]*, p. 39.
5. M. Koonen, R. Howard, R. Hansen, S. Hansen, *Sol. Phys.* **34**, 447 (1974).
6. G. Brueckner et al., *Sol. Phys.* **162**, 357 (1995).
7. V. Domingo, B. Fleck, A. Poland, *Sol. Phys.* **162**, 1 (1995).
8. B. Billings, *A Guide to the Solar Corona* (Academic Press, New York, 1966), p. 93.
9. M. Mineart, *Z. Astrophys.* **1**, 209 (1930).
10. H. Van de Hulst, *Bull. Astron. Inst. Netherlands* **11**, 135 (1950).
11. J.-P. Delaboudiniere et al., *Sol. Phys.* **162**, 291 (1995).
12. R. S. Scherrer et al., *Sol. Phys.* **162**, 101 (1995).
13. This work was carried out at the SOHO Experimenters' Analysis Facility at NASA Goddard Space Flight Center. The SOHO/LASCO data used here were produced by a consortium of the U.S. Naval Research Laboratory, Max-Planck-Institut fuer Aeronomie (Germany), Laboratoire d'Astronomie (France), and the University of Birmingham (United Kingdom). SOHO is a project of international cooperation between the European Space Agency and NASA. B. Fleck made useful suggestions for improving this manuscript. This research was funded through NASA grant number 10307.

8 April 2004; accepted 17 May 2004  
 Published online 27 May 2004;  
 10.1126/science.1098937  
 Include this information when citing this paper.